

Platform for combined heavy-ion/high-energy laser experiments (heavy-ion heated extreme states of matter)

P. Hesselbach,^{1, 2, a)} J. Lütgert,³ V. Bagnoud,^{2, 4} R. Belikov,⁵ O. Humphries,^{6, 7} B. Lindqvist,³ G. Schaumann,⁴ A. Tauschwitz,² D. Varentsov,² K. Weyrich,² B. Winkler,⁵ X. Yu,² B. Zielbauer,² D. Kraus,^{3, 6} D. Riley,⁸ Zs. Major,² and P. Neumayer^{2, b)}

¹⁾ Institut für Angewandte Physik, Goethe-Universität Frankfurt am Main, Max-von-Laue Str. 1, 60438 Frankfurt, Germany

²⁾ GSI Helmholtzzentrum für Schwerionenforschung GmbH, Planckstr. 1, 64291 Darmstadt, Germany

³⁾ Institut für Physik, Universität Rostock, Albert-Einstein-Str. 23, 18059 Rostock, Germany

⁴⁾ Institut für Kernphysik, Technische Universität Darmstadt, Schlossgartenstr. 9, 64289 Darmstadt, Germany

⁵⁾ Institut für Geowissenschaften, Goethe-Universität Frankfurt am Main, Altenhöferallee 1, 60438 Frankfurt am Main, Germany

⁶⁾ Helmholtz-Zentrum Dresden-Rossendorf, Bautzner Landstr. 400, 01328 Dresden, Germany

⁷⁾ European XFEL GmbH, Holzkoppel 4, 22869 Schenefeld, Germany

⁸⁾ Centre for Plasma Physics, School of Mathematics and Physics, Queen's University Belfast, University Road, Belfast BT7 1NN, United Kingdom

(Dated: 13 December 2023)

Insert abstract here

I. INTRODUCTION

Matter at high energy density (HED), most commonly defined by an energy density above 100 J/mm^3 (or 1 Mbar of pressure), is ubiquitous throughout the universe, making up most of the matter inside compact astrophysical objects, such as (giant) planets, brown dwarfs and stars. Theoretical description in particular of the so-called warm-dense-matter (WDM) regime, with densities around and above solid density, and electron-volt temperatures, remains a great challenge, as the potential energy between the ions, the electron chemical potential, and chemical bonding and ionization energies are all comparable to the thermal energy. WDM thus constitutes a strongly coupled, partial degenerate, partially ionized plasma, and predicting material properties, such as equation-of-state, phase boundaries, ionization, optical and transport properties, which are an important prerequisite for modeling e.g. planetary structure and evolution¹, requires computing intensive quantum many-particle calculations². Understanding of these complex matter states is also of crucial importance to applications such as inertial confinement fusion, where the fusion fuel has to pass through the WDM regime³.

Producing samples at HED conditions in the laboratory allows to experimentally test modelling of these extreme states of matter. This is enabled by powerful drivers capable of delivering energy on short timescales to small volumes. Pulsed power machines have been used to accelerate flyer plates for shock compression to Mbar pressures⁴, or for radiative heating to temperatures relevant to the study of solar opacities⁵. Large-scale laser facilities produce pressures of tens of Mbar or Gbar

via hohlraum-driven planar⁶ or spherical compression⁷. Ultra-short X-ray pulses from X-ray free electron lasers, focused to few-micron spot sizes, have been used to isochorically heat samples within femtoseconds to highly transient out-of-equilibrium states with temperatures up to 100 eV⁸.

Pulses of swift heavy ions offer an interesting alternative approach to reach HED conditions. High-energy ions passing through matter lose energy predominantly through electronic stopping, i.e. transferring energy to electrons in the target via coulomb collisions. The range of heavy ions like lead or uranium with energies of several hundred MeV per nucleon in matter at solid density is of the order of millimeters. This presents a means to volumetric heating of targets, producing large (mm^3), highly homogeneous samples of WDM.

At the international Facility for Antiproton and Ion Research (FAIR), currently under construction at the GSI Helmholtzzentrum für Schwerionenforschung near Darmstadt, Germany, the new heavy-ion synchrotron SIS-100 is foreseen to deliver pulses of relativistic heavy ions at unprecedented intensities, reaching up to several 10^{11} U-ions per pulse⁹. While a strong emphasis of the FAIR science program is on exploring the quantum chromodynamic phase diagram, exotic nuclei involved in astrophysical nucleosynthesis processes, and fundamental symmetries¹⁰, a dedicated experimental station - the "APPA-cave" - is dedicated to extreme matter research in atomic and plasma physics and for application-oriented research in biophysics, medical physics and materials science. For experiments in HED science, a set of large-bore superconducting focusing magnets will allow to focus the relativistic heavy-ion beams to sub-mm spotsizes¹¹. To illustrate the potential for volumetric heating, Fig. 1 shows the specific energy deposition of 10^{10} uranium ions, focused to a Gaussian spot with a diameter of 1 mm (FWHM). With the intensities expected at FAIR, HED conditions with temperatures in

^{a)} Electronic mail: p.hesselbach@gsi.de

^{b)} Electronic mail: p.neumayer@gsi.de

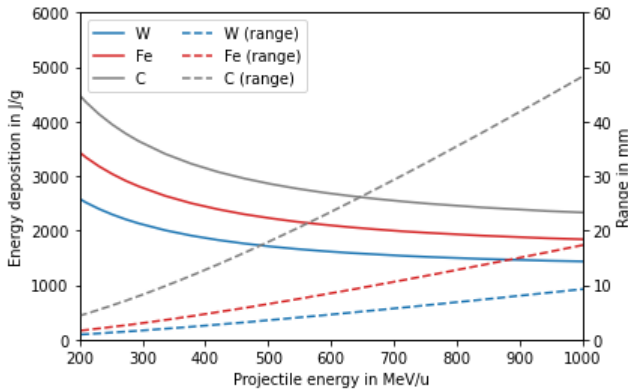


FIG. 1: Energy deposition and range of uranium ions vs. projectile energy in different materials, calculated with SRIM¹⁶. For the specific energy deposition, a total of 10^{10} ions and a Gaussian focal spot distribution with a diameter of 1 mm (FWHM) were used.

the eV range can be reached. Several schemes have been proposed for example to generate high-entropy states in the region around the critical point of metals¹² or low-entropy compression schemes to produce conditions as found in planetary interiors^{13,14}. The international collaboration HED@FAIR is coordinating the development of the scientific case and the experimental infrastructure in order to exploit these new capabilities for HED science¹⁵.

With the new facility still under construction, an important current activity is the commissioning of experimental hardware, testing of detectors, and validation of experimental approaches and schemes. These activities are pursued within the ongoing "FAIR Phase-0" at the existing HHT experimental area at GSI. To this end, in this paper we report on the commissioning activities at the newly upgraded experimental station HHT dedicated to prepare for the first HED experiments.

The paper is structured as follows: in section II we describe the experimental infrastructure at the HHT cave after the recent upgrade activities. Sections III and IV explain the diagnostics used to characterize the ion beam focus and pyrometric temperature measurements of the heavy-ion heating. Section V gives a more detailed account of the X-ray backlighting capabilities afforded by the new high-energy laser beamline to the cave, and the X-ray diagnostics commissioned. Finally, section VI will give an outlook on future plans and developments.

II. HHT EXPERIMENTAL AREA AT GSI

At GSI, the HHT experimental area is dedicated to plasma physics research. It is located downstream of the SIS-18 heavy-ion synchrotron, which has been upgraded in preparation for injection into the future SIS-100 ring of FAIR¹⁷. The characteristics of the ion bunches avail-

able in the HHT cave cover a wide range in terms of ion species, energy and time structure. On the one hand, heavy ions species (e.g. Pb or U) at moderate energies deposit large amounts of energy in the sample and can be used for HED-studies, as outlined in section I. On the other hand, light ions from protons up to carbon with energies in the GeV-range can be exploited as a powerful diagnostics for visualizing ultra-fast processes in dense matter using the PRIOR-II proton radiography facility¹⁸.

The HHT cave has recently been equipped with a laser beamline, connecting the cave with GSI's high-energy laser facility PHELIX, to enable experiments combining the intense ion beams with energetic laser pulses. The laser beamline is designed to transport nanosecond laser pulses with energies up to 200 J at a wavelength of 527nm (i.e. the second harmonic). More detail on the architecture and performance of both the laser facility and the new laser beamline can be found in [PHELIX2022]. In addition, the target chamber foreseen for the future "APPA-cave", has already now been installed at HHT (see Fig. 2). The vacuum chamber offers ample space ($> 1 \times 1\text{m}^2$) for the use of large optics required for energetic laser beams and a large number of in-vacuum diagnostics. It is built entirely of Aluminium (special alloy??) to reduce activation of the chamber walls by high-energy secondary radiation produced by the ion beam. The chamber rests on a rigid aluminium frame (ITEM). The large optical table inside the vacuum as well as breadboards outside are mounted on separate support frames, mechanically decoupled from the chamber walls, in order to minimize vibrations from vacuum pumps and movements due to inevitable deformation of the chamber walls upon pumpdown.

Reaching HED conditions requires tight focusing of the ion beam, e.g., to a focal spot size below 1 mm. At HHT, for this purpose a pair of large-aperture normal-conducting quadrupole magnets is located right in front of the target chamber. Ion-optical calculations in previous design studies [Varentsov, GSI-Report 2004] had shown that millimeter spot sizes can be achieved for ions with magnetic rigidity up to 10 Tm (e.g., U^{73+} at 350 MeV u^{-1}) over a focal length up to 1 m. Consequently, the interaction point inside the new target chamber is positioned at a distance of approximately 0.75 m from the exit of the final focusing magnet. The ion beam focal intensity distribution can be measured by imaging the optical light emitted either by beam-induced fluorescence (BIF) of a background gas, or from optical transition radiation (OTR) upon passage of the ions through a thin foil. In addition, the total number of ions is measured by means of absolutely calibrated fast current transformers (from which also the pulse duration and temporal structure of the ion bunch can be obtained). Combining these measurements yields the in-focus ion fluence distribution, which allows calculating the specific energy deposition.

In order to directly measure the temperature achieved by the heavy-ion heating, two different setups for py-

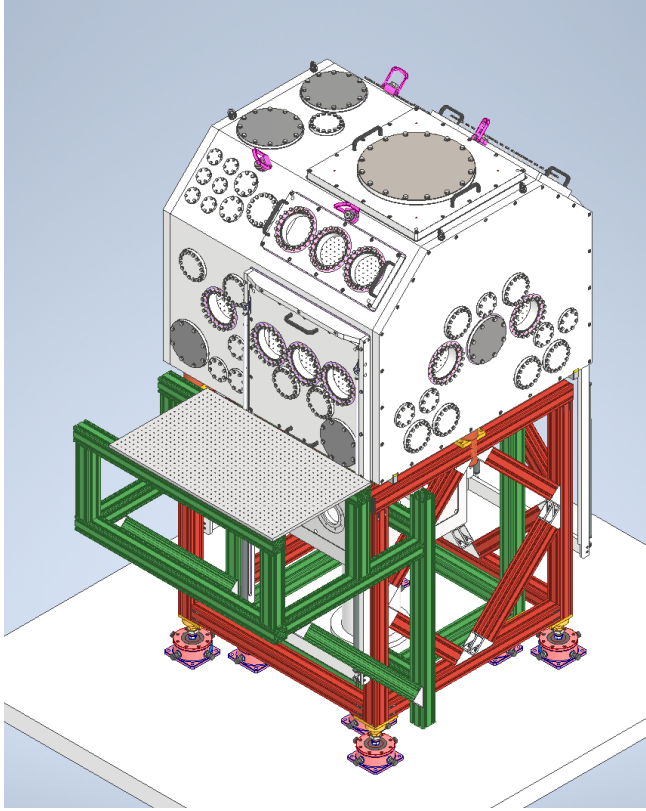
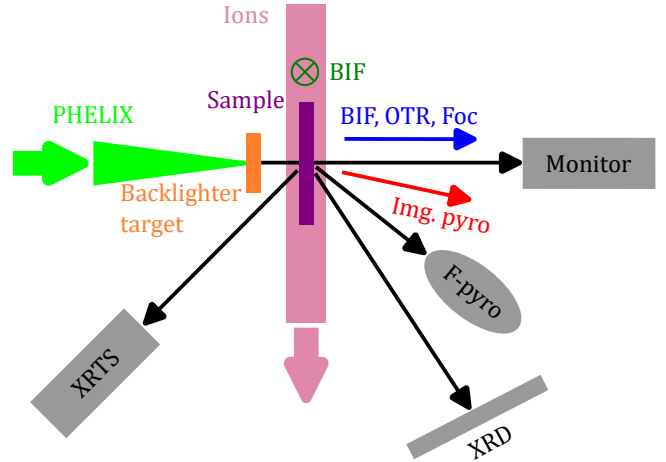


FIG. 2: The APPA target chamber on its support frame (red) and the diagnostics table support (green).

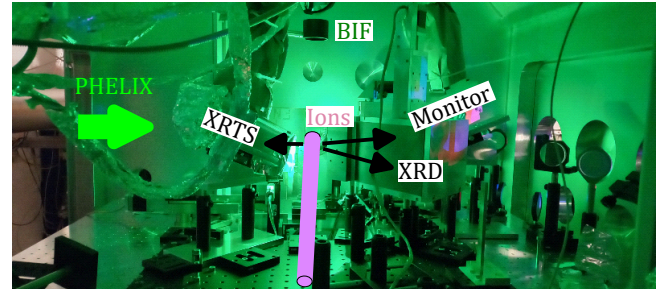
rometric temperature measurements have been implemented. Gated optical imaging allows for spatially resolved measurements of the thermal emission from the heated target. In addition, single-point measurements can be performed with a fiber-based light-collection setup, providing time-resolved measurements at up to 5 different wavelengths (between 600 nm and 1550 nm), using an array of fast photodiodes [Roman]. We will describe ion beam focal spot measurements and pyrometry measurements in Sections III and IV, respectively.

With the availability of high-energy laser pulses in the HHT cave, we are now able to apply state-of-the-art X-ray probing schemes to diagnose heavy-ion heated samples. In a first proof-of-principle experiment, we were able to demonstrate X-ray diffraction (XRD) and X-ray Thomson scattering (XRTS), measurements directly probing the microscopic structure of the sample. Performance of the laser-driven X-ray source and the design of the X-ray diagnostics is described in the following section V.

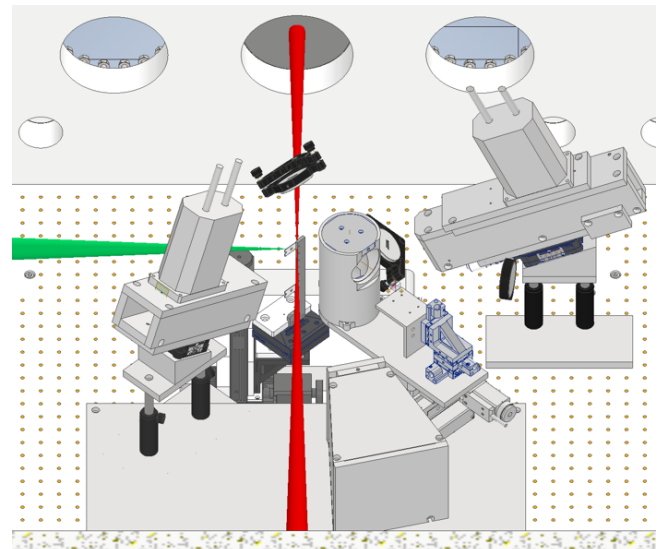
The experimental setup in the commissioning beamline is shown in Fig. 3. The targets in these first experiments, foils or thin slabs, are oriented parallel to the incoming ion beam. This results in homogeneous heating along the target, as the range of the incoming ions (here (300 – 450) MeV/u) exceeds the target dimension along the ion beam. Several optical imaging lines are used



(a) Schematic (top view) of the experimental setup.



(b) Picture of the experimental setup.



(c) CAD drawing of the experimental setup. In Stil von a und b anpassen? Ionenstrahl divergent darstellen? Tatsächliches Target einzeichnen in CAD Zeichnung?

FIG. 3: Experimental setup shown as (a) schematic topview, (b) picture and (c) CAD drawing. A PHELIX pulse is incident on the backlighter target to create X-rays for probing the ion-heated sample. X-ray diagnostics are shown along with optical diagnostics: Monitor spectrometer (Monitor), X-ray Thomson scattering spectrometer (XRTS), X-ray diffraction detector (XRD), fiber-optical pyrometry (F-pyro), imaging pyrometry (Img. pyro), beam-induced fluorescence (BIF), optical transition radiation (OTR) and laser focus diagnostics (Foc). In (b), not all of the diagnostics are visible and in (c) only the first optic of each imaging setup is shown.

to facilitate accurate target alignment, imaging of BIF and OTR to position the ion beam focus and measure its size and intensity distribution, and thermal imaging for pyrometric measurements. The PHELIX laser pulse is focused by means of an $f = 1.8\text{ m}$ lens, located outside the target chamber, onto a backscatterer target, using the imaging line opposite the incoming laser beam. X-rays emitted by the laser-generated hot plasma, located a few mm from the main target, are used to backlight the sample. A monitor spectrometer measures the x-ray yield and spectrum of the source on every shot. X-rays diffracted from the crystal lattice are detected using a well-shielded large-area detector, while the weak scattered radiation is spectrally resolved in a high-efficiency scattering spectrometer.

Hier schon X-ray section?

III. CHARACTERIZATION OF THE ION-BEAM FOCUS

In order to visualize the ion fluence distribution in the focus, we use the optical emission, produced either from beam-induced fluorescence (BIF) of a background gas fill, or optical transition radiation (OTR) of a thin foil driven into the ion focus. The emission is imaged by a combination of two infinite-conjugate achromatic lenses of 2"-diameter (*Thorlabs ACT508-300-A* and *ACT508-1000-A*, or *ACT508-250-A* and *ACT508-750-A*). The first lens is located 250 mm or 300 mm from the image plane, to allow for efficient light collection, and the second lens forms an image with 3x or 3.3x magnification onto gated intensified cameras (*PCO DiCam Pro*), located on the optical breadboards outside the target chamber. The optical resolution of the setup is limited to approximately 30 μm , due to a combination of spherical and chromatic aberrations (as found in optical raytracing simulations). **30um is experimentally determined. Whats the result from raytracing simulations? How doe we mention distances of both views nicely?**

For BIF, the target chamber is flooded with Argon gas at pressures of typ. 100 mbar. Collisional excitation by the passage of the swift heavy ions is followed by fluorescence line emission of the background gas. Previous investigations [Hampf](#) have shown that lines from neutral atoms are strongly excited by recombination processes and secondary electrons, which can lead to an emission distribution that significantly differs from the ion beam distribution. By contrast, ionic lines are found to be predominantly excited directly by heavy-ion collisions. In Argon, the strongest 4p-4s emission lines from neutral atoms (Ar I) are in the spectral range (700 – 900) nm, while the emission from ionic Argon (Ar II) lies in the spectral range from (400 – 500) nm. In our setup, we therefore have used interference bandpass filters ((450 \pm 40) nm) (*L.O.T.-Oriel*) to spectrally select emission from ionic lines. Furthermore, the excited state lifetimes of ionic lines are in the range of a few to some tens of nanoseconds, so that broadening due to thermal

motion is negligible. Figure 5a shows a typical BIF image of the ion beam at focus. As the image provides only a projection of the ion beam distribution in the viewing direction, we employ two orthogonal views to obtain the focus width in both x- and y-direction.

OTR occurs when a charged particle passes through a surface with a change of the refractive index. Being a consequence of the Maxwell-equations of electromagnetism, the emission does not involve any atomic processes, and therefore directly reflects the distribution of the ion beam. In our setup, we have implemented OTR measurements by placing a thin Aluminum foil at an angle of 45 deg w.r.t. the ion beam, using the side-view imaging line from the BIF measurements to obtain a direct image of the in-focus ion distribution. An example image is shown in Fig. x. While the 2D Gaussian-like distribution can be clearly seen, at the highest intensities we also observe a number of bright "hot-spots", which cannot be attributed to the ion beam. We speculate that these might be the result of the foil's surface structure. In the future, we plan to use thin foils of carbon or graphene, which come with a significantly smoother surface, and in addition can stand significantly higher fluences.

Figure 5 summarizes our results of the focal measurements. The OTR raw image in Fig. 5b shows an intensity distribution with some speckles, but such an ion distribution is unphysical and we believe the speckles result from the surface roughness of the Aluminum foil. Because of the worse data quality of the OTR images compared to the BIF images (see Fig. 5a), we attribute the focal widths fitted to the raw images larger statistical errors of 5 % for OTR compared to 2 % for BIF. Figure 5c shows the FWHMs of the major axes of different ion pulses measured by OTR and BIF. We observe an increase of the focal size with ion number as the occupied phase space volume increases **????**. For the highest ion numbers achievable, we have compared OTR and BIF. While in y-direction, the measurements agree within the statistical uncertainty, we observe a systematic offset in x-direction. This can be attributed to a systematic uncertainty in the tilt of the Aluminum foil and a systematic uncertainty in the spatial calibration of the optical views as BIF x-direction and OTR x-direction are not imaged by the same optical system.

Given the total number of ions and the fluence distribution in the focus, the specific energy deposited by the ion pulse in the sample can be calculated, e.g., using ion stopping powers from the software SRIM¹⁶. From this, using the temperature-dependent heat capacity and enthalpy of fusion of the target material, we can estimate the temperature increase from the heavy-ion heating. As a first crosscheck, we can predict the area across the target, where the temperature reaches or exceeds the melting temperature of the target material. This prediction can be directly compared to the holes found in a post-mortem analysis of the targets. For example, fig. 4 shows a scanning electron microscope (SEM) image of a 100 μm thick tantalum plate, after being exposed to

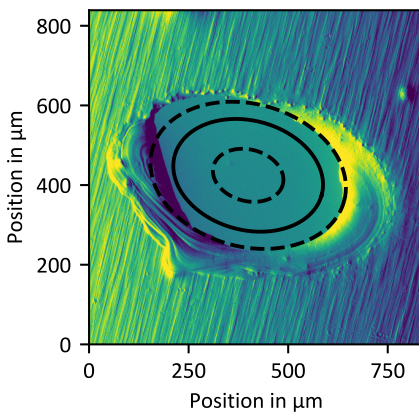


FIG. 4: SEM image of a tantalum plate, after irradiation with a single ion pulse. For comparison, the ellipses indicate the area in which the calculated temperature exceeds the melting temperature of Ta (3290 K). The dashed lines result from the assumed $\pm 10\%$ uncertainty in the total ion number. Since the rotation of the foil in the SEM is arbitrary, the ellipses are rotated to match the hole.

a single heavy-ion pulse, oriented at an angle of 45 deg to the beam. Also shown is the outline of the area, in which the temperature is calculated to exceed the melting temperature. The dashed lines show calculations varying the total ion number by $\pm 10\%$, which is the uncertainty we estimate for the beamline transmission to the target. The post-mortem analysis of the targets thus corroborates the focal fluence distribution measurements, and confirms that already with the ion beam intensities currently available at HHT, samples can be heated to several thousand degrees.

Discuss how to determine hole size.

Wie Fehler am besten bestimmen? Bayesian fitting with error being one fit parameter?

Why do we assume focus to have Gaussian distribution? What if focal spot rotated? Write about fit of Gaussians? Focal spot orientation given by orientation of quadrupoles.

IV. PYROMETRIC TEMPERATURE MEASUREMENTS OF THE HEATED SAMPLES

Standard experimental setups at HHT for the investigation of heavy-ion heated matter include pyrometric temperature measurements. These are based on the dependence of the thermal emission on the temperature and wavelength as described by Planck's radiation law. We installed a setup for imaging of the thermal emission of the heated samples, enabling space-resolved temperature measurements.

The setup consists of two achromatic lenses (*Thorlabs ACT508-300-AAC* or *ACT?*) guiding the thermal

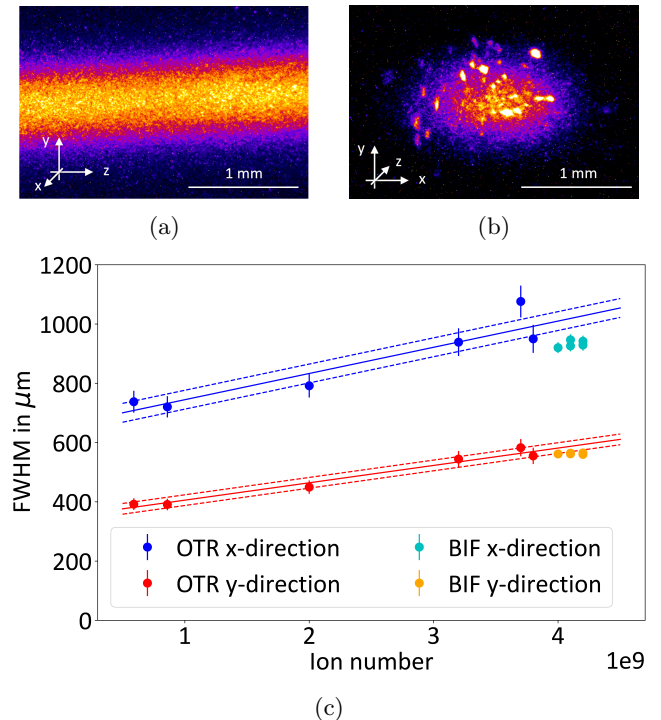
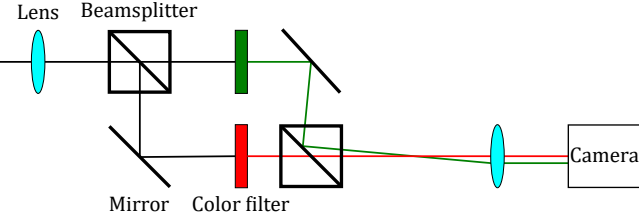


FIG. 5: Focal measurements of the heavy-ion beam by BIF and OTR. (a) raw image of BIF, (b) raw image of OTR, (c) series of measurement with up to 4×10^9 Pb ions at 300 MeV u $^{-1}$. The ion numbers refer to values measured with a fast current transformer located at the entrance of the beamline. Note that the beam propagates in z-direction.

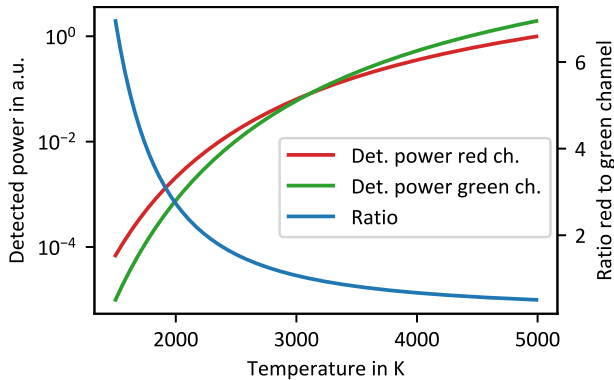
emission outside the chamber. As shown in fig. 6a, this is followed by a another set of achromatic lenses (*Thorlabs AC254-150-A???*), beam splitters (*Thorlabs BSW27*) and mirrors (*Thorlabs PF20-03-P01*) to split the thermal emission into two channels. The images of the thermal emission in both channels are detected next to each other on a gated, intensified CCD camera (*PCO DiCam Pro*).

In one of the two channels, we installed a color filter in the red wavelength range (*Thorlabs FB700-40*) enabling one-channel pyrometric measurements, the use of the other channel with a filter in the green wavelength range around 550 nm is foreseen in the near future as indicated in fig. ???. The sensitivity of the red channel was calibrated by a tungsten lamp with precisely known current-temperature dependence. As shown in Fig. 6b, the wavelength of the red channel is selected in a way that the detected power can be precisely related to the black body temperature of the sample when heated to a few thousand Kelvins. Taking into account emissivity data of the sample material allows conclusions on the real temperature.

Figure 7 shows the spatial peak temperature of our pyrometric measurements for different materials and for different ion beam intensities. The measured tempera-



(a) Scheme of the pyrometric setup including the red channel of the experiment and a foreseen green channel.



(b) Theoretical temperature dependence of the detected power in the two channels of (a) for black body emission.

FIG. 6: In (a), the experimental implementation of the pyrometric measurement is shown, in (b) the expected signal. If two channels are used, single-channel pyrometric measurements can be complemented by the ratio of the detected power which allows to directly infer a grey body temperature.

tures are shown in comparison to those expected from the energy deposition of the heavy ions simulated with SRIM taking into account temperature dependent heat capacities and the enthalpy of fusion. Expansion and heat conduction can be neglected in the relevant temperature ranges and time scales of few 10s of microseconds after the arrival of the heavy-ion pulse where our measurements took place. We confirmed the latter by finite element simulations with COMSOL and Ansys. Uncertainties of the expected temperature values are mainly due to the uncertainty of the ion beamline transmission $T = 0.8 \pm 0.08$. On the other hand, uncertainties of the measured temperature values are mainly attributed to the surface emissivity. Systematically measured emissivity data for our temperature and wavelength ranges is sparse and the uncertainty regarding the emissivity of our samples is further enhanced due to unknown surface conditions and an oblique angle of view of the imaging pyrometer onto the sample surface. We therefore assumed a relative error of 30 % for the emissivity.

NOCHMAL ZUSAMMEN AUF TRANSMISSION-SWERTE DT6 UND INNERHALB DER KAMMER SCHAUEN - SCHEINBAR KEIN TREND MIT IONEN-ZAHL ZU ERKENNEN, ABER MITTELWERT ÜBER

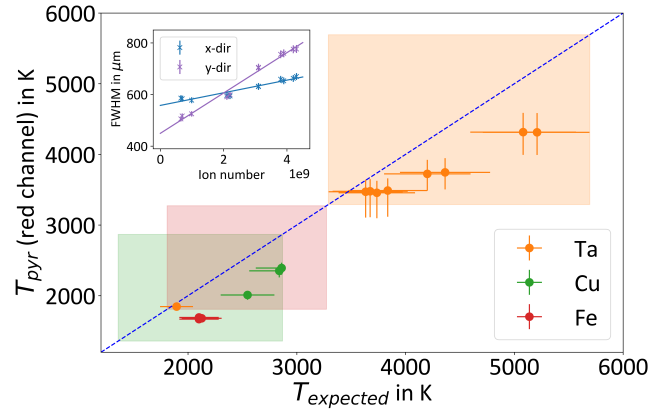


FIG. 7: The pyrometrically measured peak temperature is shown over the expected value for different materials. Rectangles mark the respective temperature ranges of the liquid phase. The dashed blue line indicates $T_{\text{pyr}} = T_{\text{expected}}$. The inset shows the ion focal distribution for the presented pyrometer data measured separately by BIF. The ion numbers refer to values measured with a fast current transformer located at the entrance of the beamline.

0.8

WIE AUSFÜRLICH SOLL DAS SEIN?
BRAUCHEN WIR EINE TABELLE ALS ÜBERSICHT
ÜBER DIE VERSCHIEDENEN TARGETS?

Generally, the measured temperatures in Fig. 7 are systematically lower than the expected values. While the Copper and Iron data has only been taken with high ion numbers (2.6-3.3e9), the Tantalum data spans a larger range of ion numbers from 4e8 to 3.3e9 ions. On the one hand, there is a good agreement between the measured and expected temperatures for low ion numbers, but on the other hand the deviation between these two temperatures increases for larger ion numbers.

This suggests that a systematic error in the calculation of the energy deposition at high ion numbers occurs: The beamline transmission might be dependent on the ion number as the occupied phase space volume changes. Future work will focus on a precise measurement of the ion number just before the target chamber.

In the case of the presented Iron data, further uncertainty is due to the fact that the target normal was rotated 90 degrees with respect to the ion beam incidence direction. The resulting irradiation of the material's edge does not guarantee to be perfectly matched to the most intense part of the ion focus despite the alignment procedure being more precise than 50μm.

We performed the pyrometric measurements presented above in a different ion beam setting than the OTR and BIF measurements presented in section III. Here, we used Pb ions with 450 MeV u⁻¹ and decelerated them by a 15 mm PMMA degrader to 288 MeV u⁻¹ according to SRIM simulations. While the higher ion energy of 450 MeV u⁻¹ instead of the default 300 MeV u⁻¹ allowed

for better focussing, the subsequent deceleration was necessary to keep the energy deposition high. BIF measurements of the ion focus in that setting are shown in the inlet of Fig. 7 along with a fit to infer the focal spot size for the calculation of the expected temperatures.

An example of a spatially resolved temperature measurement with our pyrometric setup is shown in Fig. 8 **maybe mark it in the plot above?** along with the expected distribution. The data was measured with a Tantalum sample tilted at an angle of 45 deg w.r.t. the ion beam and projected onto a surface normal to the ion beam during the analysis for better comparison with the ion focus size and the resulting temperature expectation.

As the count rate varies strongly with temperature (see Fig. 6b), the dynamic range of the temperature measurement is limited by the dynamic range of the camera. Pixels with count values below twice the standard deviation of the background are plotted grey in the 2D temperature image and line-outs. This corresponds to temperatures below **xxx K. Weiß = unter Interpolationsrange -i, auch grau machen? The measured spatial distribution of the temperature is broader than the expectation because**

To complement the spatially resolved measurements, an optical-fiber pyrometer featuring multiple channels with temporal resolution is currently being developed. **Zeigen wir das schon im setup? Wie verkaufen wir es?**

Discuss Schärfentiefe for 45deg targets as reason for broadening

V. LASER-DRIVEN X-RAY DIAGNOSTICS

Probing with X-rays has become an indispensable diagnostic tool for characterizing HED matter states produced in the laboratory. X-rays with photon energies of several to some 10s of keV are able to penetrate the dense samples, thus delivering volumetric information, and high-energy laser-produced plasmas provide sufficient X-ray flux to backlight the short-lived events. Given that large-scale laser facilities **Hier klarer machen, dass Laser eh für kompression benutzt wird?** often have a few laser beamlines "to spare", laser-produced X-ray sources are widely employed for X-ray probing. (We note that also non-laser compression facilities have opted to build dedicated laser beamlines for the purpose of enabling laser-driven X-ray diagnostics¹⁹. **On the other hand, the exceptional X-ray beam characteristics of X-ray free electron lasers motivated the setup of dedicated HED end stations (or "instruments"), featuring HED drivers such as high-energy or ultra-high intensity laser systems and pulsed magnetic fields^{20,21}.**)

High-resolution X-ray radiography provides images of the mass density distribution and thus access to the rapid hydrodynamic evolution, allowing to directly benchmark equation of state (EOS) models²². In ICF experiments, radiographic imaging is routinely used to assess the implosion performance²³. Besides merely imaging the macroscopic mass density distribution, X-ray

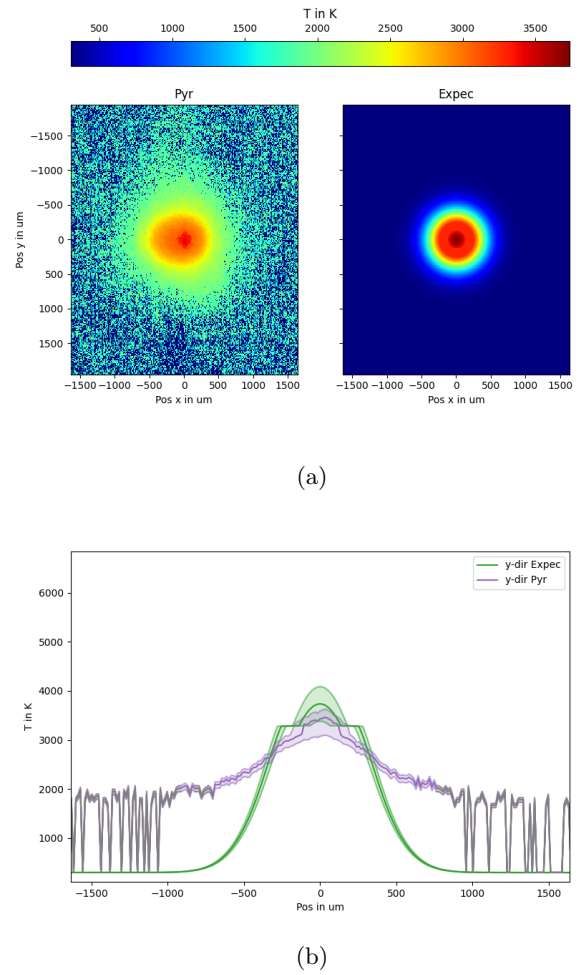


FIG. 8: Pyrometry measurement of the spatial temperature distribution in a tungsten sample.

based probing techniques also give direct access to microscopic structure, and other plasma parameters, such as temperature, charge state, and transport properties. **X-ray diffraction has been used to reveal solid-solid phase transitions (e.g.^{24,25}) and infer the lattice temperature²⁶. Spectrally resolved X-ray Thomson scattering can probe the electron velocity distribution²⁷ and plasmonic excitations²⁸.**

Given this important diagnostic capability/potential, a high-energy laser beamline is foreseen for the "APPA-cave" to enable state-of-the-art X-ray probing. In its first stage this will be a 100J-class nanosecond-pulse laser beamline, capable of producing on-target intensities of the order of 10^{15} W/cm^2 . This is sufficient to produce plasmas at keV temperatures, where collisionally excited line emission from highly charged ions reaches appreciable yields²⁹ for backlighting from XUV to X-rays with approximately 10 keV energy. These sources will enable a wide range of X-ray backlighting diagnostic schemes on lower-Z targets, such as keV radiography using pinhole

imaging, VUV opacity measurements, X-ray near-edge absorption structure, X-ray diffraction, and X-ray scattering applications.

In order to perform first proof-of-principle experiments combining intense heavy-ion pulse heated samples with laser-driven X-ray probing and advance the development of diagnostic techniques, a high-energy laser transport beamline has been built in the past 2 years to deliver high-energy nanosecond laser pulses from the laser building/bay to the HHT experiment station.

Here, we have focused a 2 ns long laser pulse with up to 200 J of energy at a wavelength of 532 nm in normal incidence onto a backlighter target using a f/13 lens. Reaching peak intensities of $1 \times 10^{16} \text{ W cm}^{-2}$, a plasma is generated and heated to few keV, predominantly by collisional absorption. Highly ionized states, such as Helium-like ions, are generated for mid-Z targets resulting in He_α line emission from collisional excitation. The laser target is located close to the heavy-ion heated sample, therefore the generated X-ray emission can be used as backlighter for diagnostics.

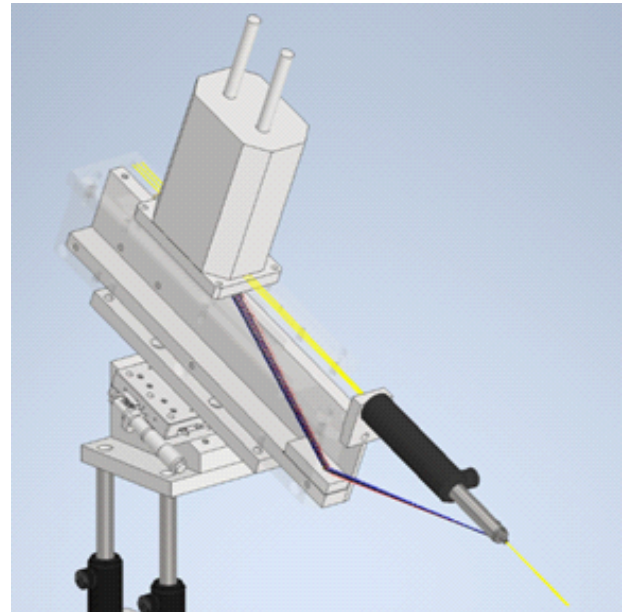
So? Oder hier die Energien komplett weg? The energy of the line emission being tunable by the choice of target material, we have exemplarily generated Titanium and Chromium He_α emission at 4750 eV and 5682 eV, respectively, and used for X-ray Thomson scattering and X-ray diffraction. The implemented XRD detector, XRTS and monitor spectrometer and our results regarding the laser-driven X-ray emission are presented below.

Mit Julian und Dominik klären: sample/target, monitor/source

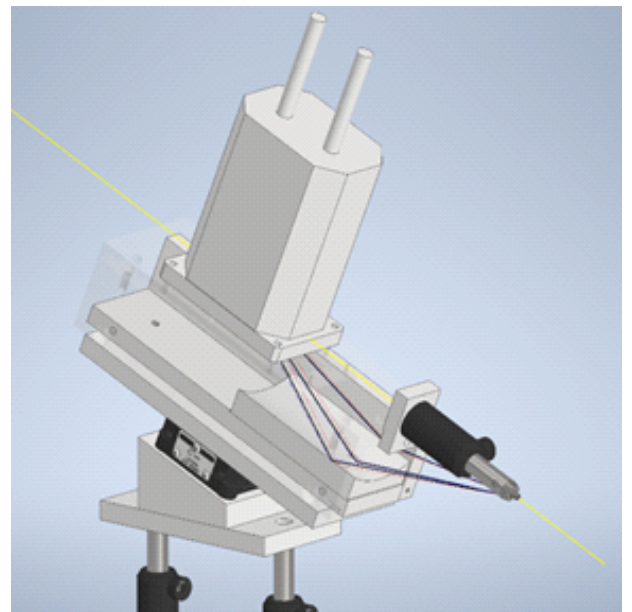
A. Monitor Spectrometer

The spectrometer is based on a Highly-Oriented Pyrolytic Graphite (HOPG) crystal (thickness 100 μm) and an X-ray CCD camera (*Greateyes GE-VAC 2048 512 BI*) as detector, both mounted to an aluminum housing as shown in Fig. 9a. To allow coverage of different spectral ranges the spectrometer length can be adjusted. To assure the focusing condition of the mosaic HOPG crystal, a length-adjustable pointer can be installed at the frontside of the spectrometer housing for the alignment procedure. It should be noted that electromagnetic pulse (EMP) issues of the camera are mitigated by shielding the camera housing as well as the power supply and data transfer cables.

The spectral range (SR) of the monitor spectrometer is limited by the CCD chip size. The length of 27.6 mm in spectral direction realizes $\Delta E_{\text{SR}} > 300 \text{ eV}$ for typical backlighters. A micrometer stage included into the spectrometer design allows for fine-adjustment of the covered spectral range. An exemplary spectrum of a Ti backlighter detected with the monitor spectrometer is shown in Fig. 10. Experimentally, we find a FWHM of 8(1) eV for the Ti He_α line. There are three main contributions to the measured linewidth: the width of the line emis-



(a) Source spectrometer



(b) XRTS spectrometer

FIG. 9: Mechanical construction of the (a) monitor and (b) XRTS spectrometer. While the mechanical setup is similar, the XRTS spectrometer features a bent crystal to increase the signal strength on the detector.

sion from the plasma itself, the source size broadening and the spectrometer resolution.

We performed simulations with the atomic physics code FLYCHK³⁰ which indicate line widths of $\sim (2 - 3)$ eV for reasonable plasma parameters of $n = n_c = 4 \times 10^{21} \text{ cm}^{-3}$ and $T = 1 \text{ keV}$. Assuming an X-ray source diameter of 100 μm , the source broadening is 2.8 eV for the Ti He-alpha line. To estimate the resolution of

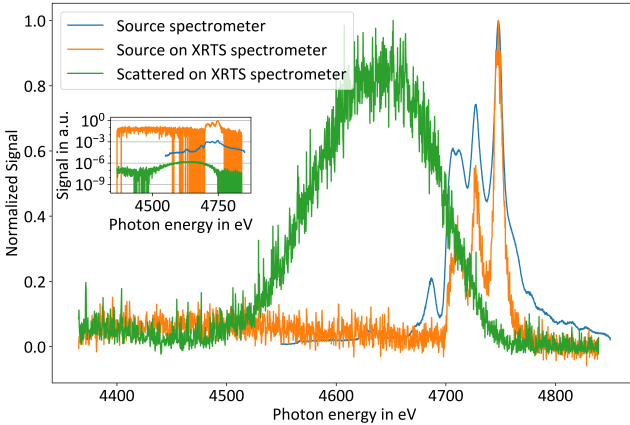


FIG. 10: X-ray spectrum generated by focusing PHELIX onto a 10 μm thick Titanium foil and detected on the source and XRTS spectrometer. Furthermore, the X-rays scattered off cold diamond, i.e., the inelastic XRTS signal, is shown (detected in a separate shot).

We note that the source spectrum on the XRTS is noisier than on the monitor spectrometer which is due to an increased sensitivity for the second diffraction order. This is, in turn, because the implemented filters to prevent saturation have higher transmission for the second than the first diffraction order. When using the XRTS spectrometer as diagnostics for scattered X-rays the filters are removed, however.

the HOPG crystal, we performed ray-tracing simulations with the code mmpxrt³¹. The simulation results show point spread functions with FWHM = 4.5 eV with depth broadening being the main contribution to the spectrometer resolution.

The monitor spectrometer is absolutely calibrated as the integrated reflectivity of the crystal as well as the quantum efficiency and analog-to-digital conversion of the camera are known. We determined the conversion efficiency from laser energy into He α line emission taking into account the whole group of lines corresponding to He 1s2 - 1s2p,s transitions as by Ruggles *et al.*²⁹. Assuming isotropic emission (and neglecting the transmission through the backlighter target ($T \sim 0.7$)), our value of $E_{\text{He}\alpha}/E_{\text{Laser}} = 2.8 \times 10^{-3}$ (for a shot with $E_{2\omega} = 78.4$ J on Ti) indicates an efficient X-ray production when comparing to $E_{\text{He}\alpha}/E_{\text{Laser}} \sim 1 \times 10^{-3}$ measured by Ruggles *et al.*

Filterdicke nochmal nachmessen?

B. X-ray Thomson scattering spectrometer

The XRTS spectrometer is based on a cylindrically-bent HOPG crystal in van-Hamos geometry³² to maximize the spectrometer's sensitivity. The crystal curvature radius $R = 50$ mm and crystal width $W = 50$ mm enable a collection efficiency of $0.39/(2\pi)$ in the non-

dispersive direction if used to detect Ti He α emission. Like the monitor spectrometer, the XRTS spectrometer features a *Greateyes GE-VAC 2048 512 BI* as detector. The length of the XRTS spectrometer is, however, shorter to increase the detected spectral range to $\Delta E_{\text{SR}} > 500$ eV in order to fully cover the inelastic Compton scattering feature.

An experimentally measured spectrum of the Titanium X-ray source on the XRTS spectrometer is shown in Fig. 10 along with a spectrum scattered off ambient diamond. For the Titanium He α line in the detected source spectrum we determined a width of FWHM = 11(1) eV. We confirmed the slightly broader line width, i.e., slightly worse resolution, compared to the monitor spectrometer by ray tracing simulations with mmpxrt³¹ which indicate a resolution of FWHM = 6.5 eV for the XRTS spectrometer. Additionally, the source broadening is increased to 4.2 eV (for a 100 μm diameter source) due to the smaller dispersion. It should be noted that the resolution of the scattered spectrum is furthermore dependent on the collimation of the X-ray backlighter source. A trade-off between resolution and signal strength is to be made, here we expect a resolution of ~ 20 eV which is currently being further analyzed.

While each spectrum is normalized in the main plot of Fig. 10, the inlet shows the relative signal strengths, taking into account the transmission of implemented filters. The bent crystal of the XRTS spectrometer increases the signal per pixel by roughly three orders of magnitude compared to the flat crystal of the monitor spectrometer, therefore enabling the detection of the six orders per magnitude weaker scattering signal. Still, only ~ 200 photons contribute to each data point of the spectrum. The large noise of the spectrum can be explained by firstly the poisson noise amounting to $1/\sqrt{200} \approx 7\%$ and secondly by counts from hard X-rays and fast electrons reaching the camera chip. Despite these intrinsic challenges for detecting the weak scattering signal, the data quality promises the capability of using XRTS as temperature diagnostics for heavy-ion heated samples, in particular with a more refined image processing which is currently being developed.

Ist wirklich zweite Beugungsordnung Ursache für größeren noise bei source on XRTS? Oder geringere Photonenanzahl? (siehe peak poisson noise) source on XRTS sieht aber nur in background noisy aus - \downarrow Weil peaks zu schmal oder wirklich so? - \downarrow Auch Photonenanzahl von brems könnte noise in background versursachen noise for scattered also from second diffraction order (but not as relevant because not filters)? and brems? not only or even rather not hard X-rays and electrons because chip is shielded against direct line of sight? - \downarrow What about fluorescence X-rays from X-rays/electrons entering housing? Poisson noise vs. noise of background How does QE influence noise?

Nochmal genauer in FLYCHK Linienbreite und Wahl der Linien für Konversionseffizienz einsteigen?

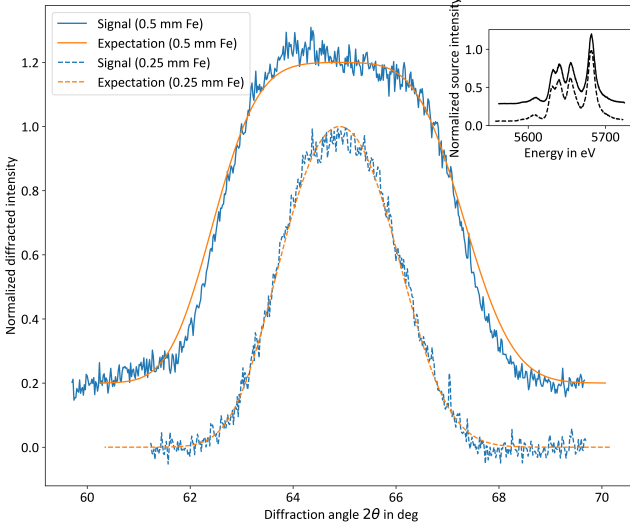


FIG. 11: Diffraction from the (110) planes of cold (BCC) iron. The width of the diffraction feature is governed by the size of the iron piece. For the larger piece, the diffraction feature and the backlighter spectrum are offset by 0.2 for better visibility.

C. X-ray diffraction setup

We have detected diffracted X-rays by an imaging plate (*Cytiva BAS IP SR 2040 E* ?) with a size of 10 cm in distances ~ 30 cm from the sample which enables to cover a large angular range of $\Delta(2\theta) = 19$ deg. In Fig. 11, the diffraction from the (110) planes of cold (BCC) polycrystalline iron is shown.

Depending on the size of the iron piece, the diffraction feature gets more or less smeared out as indicated in Fig. 11. Ultimately, the width of the diffraction feature is limited by the source size and the spectral width of the source. Convoluting all these contributions to the broadening, we have predicted the diffraction feature for two different sizes of the iron piece assuming a Gaussian X-ray source with FWHM = 60 μ m. The predictions with FWHM = 4.9 deg and FWHM = 2.6 deg, respectively, are included in Fig. 11 and compare well with the detected signal, therefore the width of the diffraction feature does not lessen its physical meaningfulness.

Due to geometrical reasons, we have used a Chromium backlighter here, resulting in slightly larger photon energies around $E_{He_\alpha} = 5682$ eV of the He_α line. The X-ray spectra detected with the monitor spectrometer of the two shots corresponding to the shown diffraction features are included in the inlet of Fig. 11. It is notable that the X-ray source is well reproducible which is beneficial for systematic studies of the sample behavior under different heating conditions by the heavy-ion beam.

VI. OUTLOOK

Where to put that?: Thanks to the flexible choice of the laser target very different X-ray sources can be realized. This includes line emission at different photon energies to which the source and XTRS spectrometer design can be easily adapted. Beyond line emission, there can also continuum or quasi-continuum X-ray emission [REF]

- ¹N. Nettelmann, B. Holst, A. Kietzmann, M. French, R. Redmer, and D. Blaschke, *The Astrophysical Journal* **683**, 1217 (2008).
- ²J. Clérouin, V. Recoules, and F. Soubiran, *Contributions to Plasma Physics* **61**, 1 (2021).
- ³J. D. Lindl, P. Amendt, R. L. Berger, S. G. Glendinning, S. H. Glenzer, S. W. Haan, R. L. Kauffman, O. L. Landen, and L. J. Suter, *Physics of Plasmas* **11**, 339 (2004).
- ⁴M. D. Knudson, M. P. Desjarlais, A. Becker, R. W. Lemke, K. R. Cochrane, M. E. Savage, D. E. Bliss, T. R. Mattsson, and R. Redmer, *Science* **348**, 1455 (2015).
- ⁵J. E. Bailey, T. Nagayama, G. P. Loisel, G. A. Rochau, C. Blanchard, J. Colgan, P. Cosse, G. Fauquier, C. J. Fontes, F. Gilleron, I. Golovkin, S. B. Hansen, C. A. Iglesias, D. P. Kilcrease, J. J. Macfarlane, R. C. Mancini, S. N. Nahar, C. Orban, J.-C. Pain, A. K. Pradhan, M. Sherrill, and B. G. Wilson, (2014), 10.1038/nature14048.
- ⁶R. F. Smith, J. H. Eggert, R. Jeanloz, T. S. Duffy, D. G. Braun, J. R. Patterson, R. E. Rudd, J. Biener, A. E. Lazicki, A. V. Hamza, J. Wang, T. Braun, L. X. Benedict, P. M. Celliers, and G. W. Collins, (2014), 10.1038/nature13526.
- ⁷A. L. Kritcher, D. C. Swift, T. Döppner, B. Bachmann, L. X. Benedict, G. W. Collins, J. L. DuBois, F. Elsner, G. Fontaine, J. A. Gaffney, S. Hamel, A. Lazicki, W. R. Johnson, N. Kostinski, D. Kraus, M. J. MacDonald, B. Maddox, M. E. Martin, P. Neu-mayer, A. Nikroo, J. Nilsen, B. A. Remington, D. Saumon, P. A. Sterne, W. Sweet, A. A. Correa, H. D. Whitley, R. W. Falcone, and S. H. Glenzer, *Nature* **584**, 51 (2020).
- ⁸S. M. Vinko, O. Cricosta, B. I. Cho, K. Engelhorn, H.-K. Chung, C. R. D. Brown, T. Burian, J. Chalupsky '5, C. Chalupsky '5, R. W. Falcone, C. Graves, V. Hájková, A. Higginbotham, L. Juha, J. Krzywinski, H. J. Lee, M. Messerschmidt, C. D. Murphy, Y. Ping, A. Scherz, W. Schlotter, S. Toleikis, J. J. Turner, L. Vysin, T. Wang, B. Wu, U. Zastrau, D. Zhu, R. W. Lee, P. A. Heimann, B. Nagler, and J. S. Wark, *Physics ASCR* **2** (2012), 10.1038/nature10746.
- ⁹P. Spiller, R. Balss, P. Bartolome, J. Blaurock, U. Blell, O. Boine-Frankenheim, L. Bozyk, M. Chorowski, T. Eiselt, M. Frey, T. Giacomini, F. Kaether, H. Khodzhibagyan, S. Klammes, H. Klingbeil, H. G. Koenig, V. Kornilov, P. Kowina, D. Lens, J. P. Meier, D. Ondreka, I. Petzenhauser, V. Plyusnin, I. Pongrac, N. Pyka, V. Raginel, P. Rottlaender, C. Roux, J. Schmidt, M. Schwickerdt, K. Sugita, A. Szwangruber, P. Szwangruber, R. Trockel, A. Waldt, H. Welker, S. Wilfert, T. Winkler, and D. Winters, *Journal of Instrumentation* **15**, T12013 (2020).
- ¹⁰M. Durante, P. Indelicato, B. Jonson, V. Koch, K. Langanke, U.-G. Meißner, E. Nappi, T. Nilsson, T. Stöhlker, E. Widmann, and M. Wiescher, *Physica Scripta* **94**, 033001 (2019).
- ¹¹T. Stöhlker, V. Bagnoud, K. Blaum, A. Blazevic, A. Bräuning-Demian, M. Durante, F. Herfurth, M. Lestinsky, Y. Litvinov, S. Neff, R. Pleskac, R. Schuch, S. Schippers, D. Severin, A. Tauschwitz, C. Trautmann, D. Varentsov, and E. Widmann, *Nuclear Instruments and Methods in Physics Research Section B: Beam Interactions with Materials and Atoms* **365**, 680 (2015).
- ¹²V. Mintsev, V. Kim, I. Lomonosov, D. Nikolaev, A. Ostriv, N. Shilkin, A. Shutov, V. Ternovoi, D. Yuriev, V. Fortov, A. Golubev, A. Kantsyrev, D. Varentsov, and D. H. H. Hoffmann, *Contrib. Plasma Phys* **56**, 281 (2016).

- ¹³N. A. Tahir, T. Stöhlker, A. Shutov, I. V. Lomonosov, V. E. Fortov, M. French, N. Nettelmann, R. Redmer, A. R. Piriz, C. Deutsch, Y. Zhao, P. Zhang, H. Xu, G. Xiao, and W. Zhan, *New Journal of Physics* **12**, 073022 (2010).
- ¹⁴N. A. Tahir, I. V. Lomonosov, B. Borm, A. R. Piriz, A. Shutov, P. Neumayer, V. Bagnoud, and S. A. Piriz, *The Astrophysical Journal Supplement Series* **232**, 1 (2017).
- ¹⁵K. Schoenberg, V. Bagnoud, A. Blazevic, V. E. Fortov, D. O. Gericke, A. Golubev, D. H. Hoffmann, D. Kraus, I. V. Lomonosov, V. Mintsev, S. Neff, P. Neumayer, A. R. Piriz, R. Redmer, O. Rosmej, M. Roth, T. Schenkel, B. Sharkov, N. A. Tahir, D. Varentsov, and Y. Zhao, *Physics of Plasmas* **27** (2020), 10.1063/1.5134846.
- ¹⁶J. F. Ziegler, M. D. Ziegler, and J. P. Biersack, *Nuclear Instruments and Methods in Physics Research, Section B: Beam Interactions with Materials and Atoms* **268**, 1818 (2010).
- ¹⁷P. J. Spiller, R. Balss, A. Bleile, L. Bozyk, J. V. Ceballos, T. Eisel, E. Fischer, P. Forck, P. Hülsmann, M. Kauschke, O. Kester, P. Kowina, H. Kollmus, H. Klingbeil, A. Krämer, H. G. König, J. P. Meier, A. Mierau, C. Omet, D. Ondreka, N. Pyka, H. Ramakers, P. Schnizer, H. Welker, S. Wilfert, D. Urner, H. G. Khodzibagyan, and A. Illuk, *IPAC 2014: Proceedings of the 5th International Particle Accelerator Conference*, 1857 (2014).
- ¹⁸D. Varentsov, O. Antonov, A. Bakhmutova, C. W. Barnes, A. Bogdanov, C. R. Danly, S. Efimov, M. Endres, A. Fertman, A. A. Golubev, D. H. Hoffmann, B. Ionita, A. Kantsyrev, Y. E. Krasic, P. M. Lang, I. Lomonosov, F. G. Mariam, N. Markov, F. E. Merrill, V. B. Mintsev, D. Nikolaev, V. Panyushkin, M. Rodionova, M. Schanz, K. Schoenberg, A. Semennikov, L. Shestov, V. S. Skachkov, V. Turtikov, S. Udrea, O. Vasyljev, K. Weyrich, C. Wilde, and A. Zubareva, *Review of Scientific Instruments* **87** (2016), 10.1063/1.4941685, arXiv:1512.05644.
- ¹⁹P. Rambo, J. Schwarz, M. Schollmeier, M. Geissel, I. Smith, M. Kimmel, C. Speas, J. Shores, D. Armstrong, J. Bellum, E. Field, D. Kletecka, and J. Porter, in *Proc. SPIE*, Vol. 10014 (2016) p. 100140Z.
- ²⁰B. Nagler, B. Arnold, G. Bouchard, R. F. Boyce, R. M. Boyce, A. Callen, M. Campell, R. Curiel, E. Galtier, J. Garofoli, E. Granados, J. Hastings, G. Hays, P. Heimann, R. W. Lee, D. Milathianaki, L. Plummer, A. Schropp, A. Wallace, M. Welch, W. White, Z. Xing, J. Yin, J. Young, U. Zastraub, and H. J. Lee, *Nature* **22**, 520 (2015).
- ²¹U. Zastraub, K. Appel, C. Baehitz, O. Baehr, L. Batchelor, A. Berghäuser, M. Banjafar, E. Brambrink, V. Cerantola, T. E. Cowan, H. Damker, S. Dietrich, S. Di Dio Cafiso, J. Dreyer, H.-O. Engel, T. Feldmann, S. Findeisen, M. Foese, D. Fulla-Marsa, S. Göde, M. Hassan, J. Hauser, T. Herrmannsdörfer, H. Höppner, J. Kaa, P. Kaever, K. Knöfel, Z. Konopková, A. Laso Garc\'ia, H.-P. Liermann, J. Mainberger, M. Makita, E.-C. Martens, E. E. McBride, D. Möller, M. Nakatsutsumi, A. Pelka, C. Plueckthun, C. Prescher, T. R. Preston, M. Röper, A. Schmidt, W. Seidel, J.-P. Schwinkendorf, M. O. Schoelmerich, U. Schramm, A. Schropp, C. Strohm, K. Sukharnikov, P. Talkovski, I. Thorpe, M. Toncian, T. Toncian, L. Wollenweber, S. Yamamoto, and T. Tschentscher, *Journal of Synchrotron Radiation* **28**, 1393 (2021).
- ²²T. Döppner, D. C. Swift, A. L. Kritcher, B. Bachmann, G. W. Collins, D. A. Chapman, J. Hawrelak, D. Kraus, J. Nilsen, S. Rothman, L. X. Benedict, E. Dewald, D. E. Fratanduono, J. A. Gaffney, S. H. Glenzer, S. Hamel, O. L. Landen, H. J. Lee, S. LePape, T. Ma, M. J. McDonald, A. G. MacPhee, D. Milathianaki, M. Millot, P. Neumayer, P. A. Sterne, R. Tommasini, and R. W. Falcone, *Phys. Rev. Lett.* **121**, 25001 (2018).
- ²³E. L. Dewald, R. Tommasini, A. Mackinnon, A. MacPhee, N. Meezan, R. Olson, D. Hicks, S. LePape, N. Izumi, K. Fournier, M. A. Barrios, S. Ross, A. Pak, T. Döppner, D. Kalantar, K. Opachich, R. Rygg, D. Bradley, P. Bell, A. Hamza, B. Dzenitis, O. L. Landen, B. MacGowan, K. LaFortune, C. Widmayer, B. Van Wonterghem, J. Kilkenny, M. J. Edwards, J. Atherton, and E. I. Moses, *Journal of Physics: Conference Series* **688**, 012014 (2016).
- ²⁴D. H. Kalantar, J. F. Belak, G. W. Collins, J. D. Colvin, H. M. Davies, J. H. Eggert, T. C. Germann, J. Hawrelak, B. L. Holian, K. Kadau, P. S. Lomdahl, H. E. Lorenzana, M. A. Meyers, K. Rosolankova, M. S. Schneider, J. Sheppard, J. S. Stölken, and J. S. Wark, *Physical Review Letters* **95**, 1 (2005).
- ²⁵M. Millot, F. Coppari, J. Ryan Rygg, A. Correa Barrios, S. Hamel, D. C. Swift, and J. H. Eggert, *Nature* 10.1038/s41586-019-1114-6.
- ²⁶T. G. White, J. Vorberger, C. R. D Brown, B. J. B Crowley, P. Davis, S. H. Glenzer, J. W. O Harris, D. C. Hochhaus, S. Le Pape, T. Ma, C. D. Murphy, P. Neumayer, L. K. Pattison, S. Richardson, D. O. Gericke, and G. Gregori, 10.1038/srep00889.
- ²⁷H. J. Lee, P. Neumayer, J. Castor, T. Döppner, R. W. Falcone, C. Fortmann, B. A. Hammel, A. L. Kritcher, O. L. Landen, R. W. Lee, D. D. Meyerhofer, D. H. Munro, R. Redmer, S. P. Regan, S. Weber, and S. H. Glenzer, *Phys. Rev. Lett.* **102**, 115001 (2009).
- ²⁸S. H. Glenzer, O. L. Landen, P. Neumayer, R. W. Lee, K. Widmann, S. W. Pollaine, R. J. Wallace, G. Gregori, A. Höll, T. Bornath, R. Thiele, V. Schwarz, W.-D. Kraeft, and R. Redmer, *Physical Review Letters* **98**, 065002 (2007).
- ²⁹L. E. Ruggles, J. L. Porter, P. K. Rambo, W. W. Simpson, M. F. Vargas, G. R. Bennett, and I. C. Smith, *Review of Scientific Instruments* **74**, 2206 (2003).
- ³⁰H. K. Chung, M. H. Chen, W. L. Morgan, Y. Ralchenko, and R. W. Lee, *High Energy Density Physics* **1**, 3 (2005).
- ³¹M. Šmid, X. Pan, and K. Falk, *Computer Physics Communications* **262**, 107811 (2021).
- ³²O. Renner and F. B. Rosmej, *Matter and Radiation at Extremes* **4** (2019), 10.1063/1.5086344.